Japanese Journal of Applied Physics

REGULAR PAPER

A study on differentiation of depiction between scatterer and reflector to assist epidural anesthesia by ultrasound

Japanese Journal of Applied Physics **60**, SDDE15 (2021) **REGULAR PAPER**
https://doi.org/**10.35848/1347-4065/abf4a3**

A study on differentiation of depiction between scatterer and reflector to assist epidural anesthesia by ultrasound

Takumi Hashimoto[1], Shohei Mori[2], Mototaka Arakawa[1,2*], Eiko Onishi[3], Masanori Yamauchi[3], and Hiroshi Kanai[1,2]

[1]*Graduate School of Biomedical Engineering, Tohoku University, Sendai 980-8579, Japan*
[2]*Graduate School of Engineering, Tohoku University, Sendai 980-8579, Japan*
[3]*Department of Anesthesiology and Perioperative Medicine, Tohoku University School of Medicine, Sendai 980-8575, Japan*

[*]E-mail: arakawa@ecei.tohoku.ac.jp

Received December 4, 2020; revised March 10, 2021; accepted April 2, 2021; published online April 28, 2021

A sharp depiction of the puncture point of the needle by differentiating muscle and bone is required for ultrasound-guided epidural anesthesia in the thoracic spine. In the present paper, we proposed a method for depicting the thoracic vertebral surface by utilizing the difference between scattering and reflection characteristics. This method estimates whether an object is a scatterer or a reflector referring to the scattering and reflection characteristics acquired in the water tank experiment. The proposed method was applied to basic experiments and in vivo experiments. In the basic experiments, the matching using root mean squared error allowed us to differentiate the depiction between scattering and reflection. In the in vivo experiment, we were able to estimate the position of the bone as a reflector and the slope was generally correct.

1. Introduction

Epidural anesthesia is one of the local anesthesia before surgery. It is often used in combination with general anesthesia because it has a great advantage in reducing the burden of patients both intraoperatively and postoperatively.[1)] The anesthesia needle is inserted into the spinal gap through the skin surface. In epidural anesthesia, especially in the thoracic spine, it is difficult to inject the needle into the proper position because of the narrow spinal gap. Currently, the success of anesthesia strongly depends on the skill of the physician, since the puncture position is mainly detected by palpation. The failure rate of epidural anesthesia has been reported to be 6%–25%.[2–4)] At the time of epidural anesthesia, 22% and 14% of patients reported back pain and psychological distress, respectively.[5)] Moreover, the failure of anesthesia leads to headaches and complications.

Medical ultrasound is used to identify the puncture position before anesthesia as an aid of palpation in the clinic.[6)] Epidural anesthesia for the lumbar spine and other local anesthesia techniques, such as the iliac inguinal gastric block and the femoral nerve block, are commonly used with ultrasound guidance.[7–10)] However, medical ultrasound does not provide a clear image of the puncture location for patients with deep spinal positions, such as obese patients.[11–13)] Studies aimed at ultrasound guidance of epidural anesthesia, such as automatic identification of the spine, have been proposed,[14–16)] but these studies have been aimed to apply on the lumbar spine, which has a wide gap and a simple structure.

Ultrasound imaging of bone has been studied in the field of orthopedics.[17–21)] For example, some methods have been proposed to identify the shape of the bone using the strain of the pressurized bones,[22,23)] phase symmetry,[24)] or shadow peaks.[25)] However, it is difficult to apply these methods to the thoracic spine because it is located deep from the skin surface and has a complex surface structure.

We have been studying the imaging methods to accurately guide epidural anesthesia for the thoracic spine. The aim is to suppress the depiction of muscle and emphasize that of bone to sharply depict the position of the needle insertion, and two methods were previously proposed. The first was to improve the misalignment of the delayed addition that occurs in the ultrasound reflected from the thoracic spine surface.[26)] This method depicts a smooth and tilted object by considering the transmitting and receiving positions not to be the same based on the envelope method[27)] and the range point migration method.[28,29)] The other method utilized the different ultrasound properties between soft tissues and bone.[30)] In this method, the ratio of an averaged delayed sum in a wide region around the ideal delay time to an ordinary delayed sum was calculated and multiplied to the luminance value of the B-mode image. As a result, we succeeded in suppressing the depiction of muscle and soft tissues for the most part, but some muscle tissues still remained. A problem of the proposed method in a previous study[30)] was to calculate the average power of the enveloped signals in the depth direction. Therefore, the previous method also enhanced the depiction of the objects other than the bones such as the scatterers around them and the dense muscle tissues when reflected waves from the objects other than the observation point were involved within the averaged region. In the present study, we investigate the scattering and reflection properties of ultrasound for muscle and bone in more detail. We have succeeded in estimating the inclination of a plane reflector by the normalized cross-correlation, utilizing that the reflection property of ultrasound shifts to angle direction according to the inclination of the reflector.[31)] However, the differentiation of the depiction of scattering and reflection was not investigated. The purpose of the present paper is to clearly depict the thoracic spine gap, which is the puncture location, by differentiating between scatterers and reflectors in the depiction. We compare the estimation results of a scatterer and a reflector by the normalized cross-correlation and the root means square error (RMSE), and apply the proposed method in in vivo experiments.

2. Principle and experimental method

2.1. Difference between scattering and reflection of ultrasound

Figure 1 shows schematic diagrams of the scattering and reflection of ultrasound waves when a focused wave is

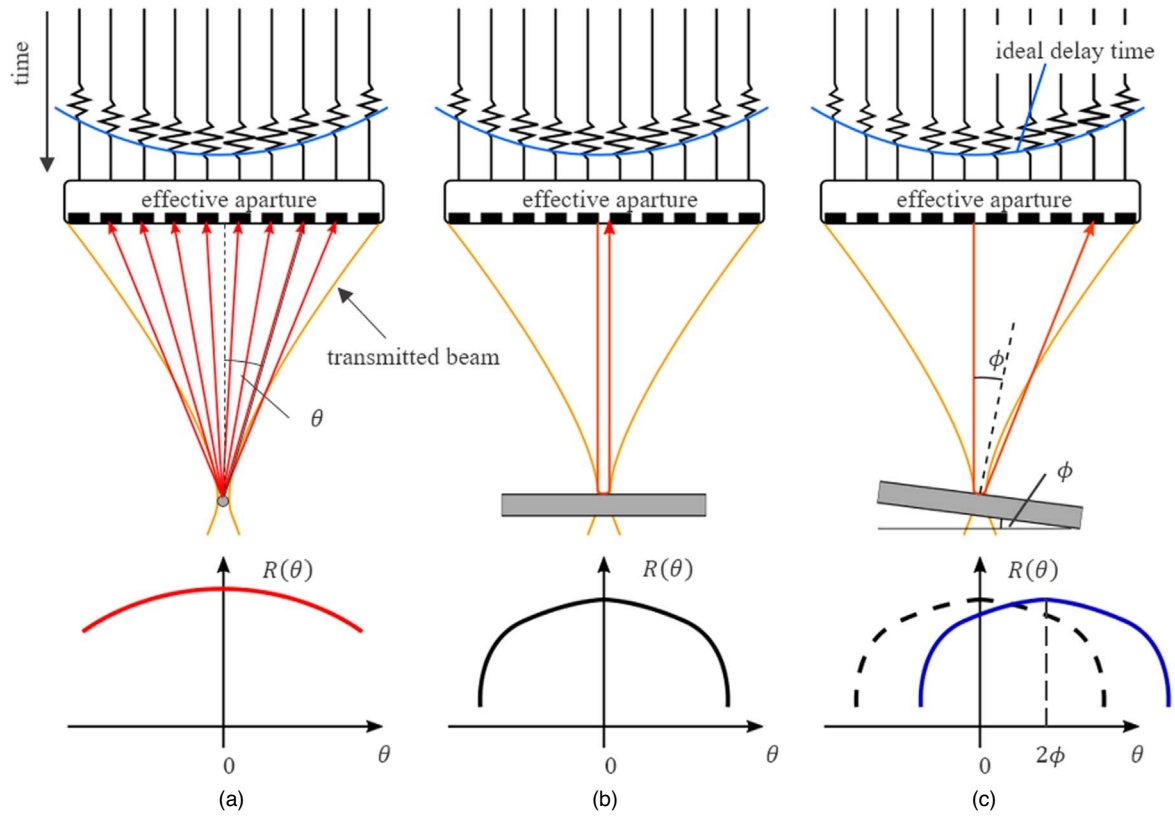

Fig. 1. (Color online) Differences in angular amplitude characteristics due to scattering and reflection of ultrasound. (a) Scattering characteristics, (b) reflection characteristics parallel to the probe, and (c) reflection characteristics tilted to the probe.

transmitted by a linear probe. Here, θ is the prospective angle from the surface of the object to the receiver element of the probe. The angular amplitude characteristics of the received signals are different for a scatterer, such as muscle tissue, and a reflector, such as bone. When a focused ultrasound is transmitted to a scattering object, as shown in Fig. 1(a), the ultrasound wave is scattered on the surface of the object in all directions. The angular dependence of scattering from a point scatterer is assumed to follow the Rayleigh scattering. The element also has a directivity when receiving scattered waves. However, since the prospective angle θ from the scatterer to the receiving element is small in the present study, the angular dependence of the amplitude characteristic $R(\theta)$ of the received signal is small in scattering. On the other hand, when a focused ultrasound is irradiated to an object with the surface structure parallel to the probe, as shown in Fig. 1(b), the ultrasound wave is specularly reflected on the object surface. The amplitude of the signal received at each element is large in the reflection direction and small in the other directions. Therefore, the angular dependence $R(\theta)$ is large in reflection.[32)]

The reflection characteristics also depend on the inclination of the reflector to the probe. As shown in Fig. 1(c), when focused ultrasound is transmitted to an object surface tilted with an angle ϕ to the probe surface, the direction of the main lobe of the refection beam is shifted by 2ϕ in the θ-axis direction. As a result, the angular amplitude characteristics of the received signal $R(\theta)$ change with the structure and the inclination of the target.

2.2. Proposed method

Figure 2 shows the schematic view of the procedure to estimate the slope of an object at a position P(x, z).[31)] $R(\theta)$ differs in scattering and reflection, and it also depends on the angle of the reflector because the transmitted beam has a width even at a focal point. First, the amplitudes on the ideal delay time corresponding to the reception time of the scattered wave, which is obtained when a point scatterer is assumed to exist at a position P(x, z), are extracted from the measured data of the ultrasonic probe before the delay-and-sum processing, and the angular amplitude characteristic $R(\theta; \mathrm{P})$ is calculated (Step I). By matching the obtained characteristic $R(\theta; \mathrm{P})$ with the scattering characteristic $R_\mathrm{S}(\theta; z_\mathrm{R})$ and the reflection characteristics group $\{R_\mathrm{R}(\theta; z_\mathrm{R}, \phi)\}$, which were obtained in a water-tank experiment in advance, we estimate whether the object is the scatterer or the reflector, and its angle if it was estimated as the reflector (Step II). The reference data was acquired so that the focal depth of the focused wave was equal to the depth of the object, z_R. Two methods were investigated for the matching. The first one is the normalized cross correlation. The normalized cross correlation with the reference data of the scattering property and the reference data of the reflection properties are shown in Eqs. (1) and (2), respectively.

$$r_\mathrm{S}(\mathrm{P}) = \frac{1}{N\sigma_\mathrm{P}\sigma_\mathrm{S}}\sum_\theta w(\theta)\{R(\theta; \mathrm{P}) - \overline{R(\theta; \mathrm{P})}\} \times \{R_\mathrm{S}(\theta; z_\mathrm{R}) - \overline{R_\mathrm{S}(\theta; z_\mathrm{R})}\}, \quad (1)$$

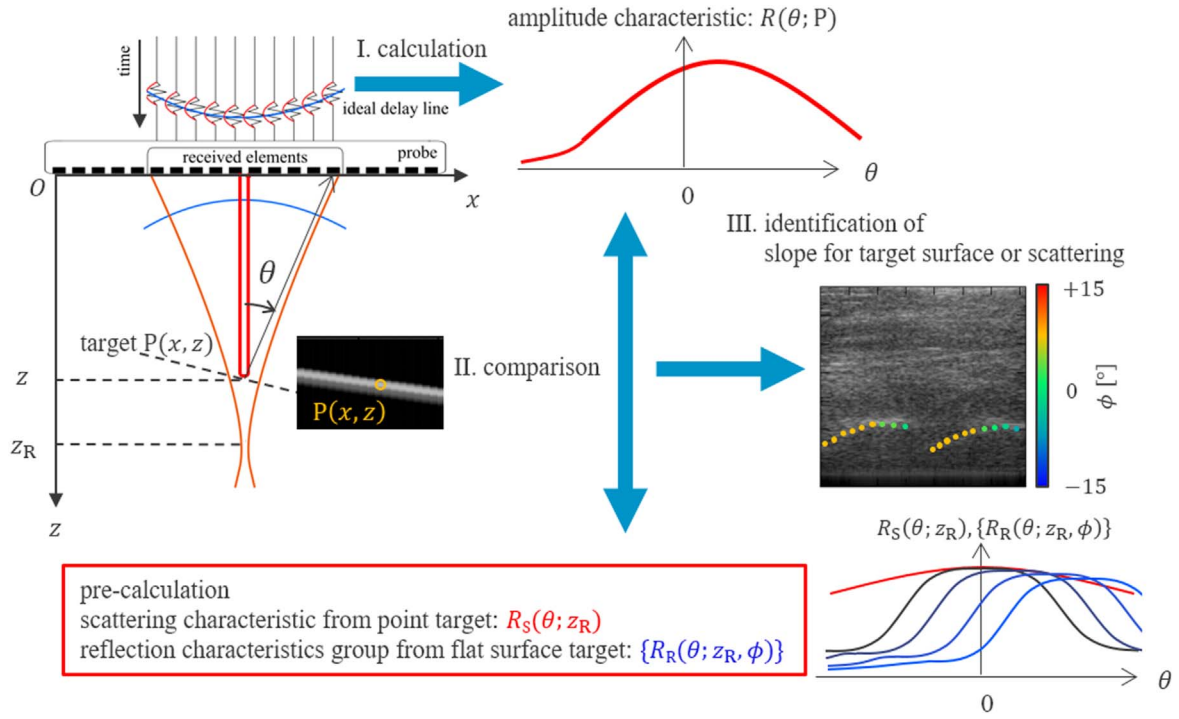

Fig. 2. (Color online) Flow of estimating the slope of an object.

$$r_R(\phi;\mathrm{P}) = \frac{1}{N\sigma_P\sigma_{R,\phi}}\sum_\theta w(\theta)\{R(\theta;\mathrm{P}) - \overline{R(\theta;\mathrm{P})}\} \times \{R_R(\theta; z_R, \phi) - \overline{R_R(\theta; z_R, \phi)}\}, \quad (2)$$

$$\sigma_P = \sqrt{\frac{1}{N}\sum_\theta [w(\theta)\{R(\theta;\mathrm{P}) - \overline{R(\theta;\mathrm{P})}\}^2]}, \quad (3)$$

$$\sigma_S = \sqrt{\frac{1}{N}\sum_\theta [w(\theta)\{R_S(\theta; z_R) - \overline{R_S(\theta; z_R)}\}^2]}, \quad (4)$$

$$\sigma_{R,\phi} = \sqrt{\frac{1}{N}\sum_\theta [w(\theta)\{R_R(\theta; z_R, \phi) - \overline{R_R(\theta; z_R, \phi)}\}^2]}, \quad (5)$$

where $\bar{R}$ is the mean value of the amplitude angle characteristics, σ is the standard deviation of the amplitude angle characteristics, and $w(\theta)$ is the window function for weighting the correlation. In the present study, we used a rectangular window with a value of 1 for all θ. The normalized cross correlation can evaluate the similarity regardless of the amplitude component by removing the DC component of the amplitude and normalizing it by the standard deviation. The object and the angle are estimated from the matching result in which the measured amplitude characteristic is the highest correlation with the reference data.

The second matching method is based on calculating the RMSE. Equations (6) and (7) show the RMSEs with the reference data of the scattering characteristics and the reference data of the reflection characteristics, respectively.

$$RMSE_S(\mathrm{P}) = \sqrt{\frac{\sum_\theta w(\theta)\{R(\theta;\mathrm{P}) - \hat{A}_S(\mathrm{P})R_S(\theta; z_R)\}^2}{\sum_\theta w(\theta)\{R(\theta;\mathrm{P})\}^2}}, \quad (6)$$

$$RMSE_R(\phi;\mathrm{P}) = \sqrt{\frac{\sum_\theta w(\theta)\{R(\theta;\mathrm{P}) - \hat{A}_R(\phi;\mathrm{P})R_S(\theta; z_R)\}^2}{\sum_\theta w(\theta)\{R(\theta;\mathrm{P})\}^2}}, \quad (7)$$

$$\hat{A}_S(\mathrm{P}) = \frac{\sum_\theta w(\theta)R(\theta;\mathrm{P})R_S(\theta; z_R)}{\sum_\theta w(\theta)\{R_S(\theta; z_R)\}^2}, \quad (8)$$

$$\hat{A}_R(\phi;\mathrm{P}) = \frac{\sum_\theta w(\theta)R(\theta;\mathrm{P})\,R_R(\theta; z_R, \phi)}{\sum_\theta w(\theta)\{R_R(\theta; z_R, \phi)\}^2}, \quad (9)$$

where $\hat{A}_S(\mathrm{P})$ and $\hat{A}_R(\phi;\mathrm{P})$ are the parameters to minimize the RMSE between the two characteristics. Using $\partial RMSE_S(\mathrm{P})/\partial A_S(\mathrm{P}) = 0$ and $\partial RMSE_R(\phi;\mathrm{P})/\partial A_R(\phi;\mathrm{P}) = 0$, we can calculate $\hat{A}_S(\mathrm{P})$ and $\hat{A}_R(\phi;\mathrm{P})$. The window function $w(\theta)$ for weighting the RMSE is the same as that for the normalized cross correlation. The object and the angle are estimated from the matching result in which the value of the RMSE between the measured amplitude characteristic and the reference data is the lowest.

The estimated results are superimposed on each point P(x, z) in the B-mode image (Step III). Accordingly, this method will locally estimate whether an object is a scatterer or a reflector. The previous method calculated the average of the power of the enveloped signal for 9 wavelengths in the

depth direction.[30] In contrast, this method uses only the enveloped amplitudes of the ideal delay time. Therefore, this method can greatly reduce the effect of the reflected waves from the objects other than the observation point P(x, z) compared to the previous method.

2.3. Experimental method

The purpose of the present study is to differentiate the depiction of scattering and reflection by using the received signals from a scatterer and a reflector acquired in the water-tank experiments as reference data. We estimated the object using data acquired from the basic experiments and in vivo experimental results for human thoracic vertebrae. The ultrasonic diagnostic apparatus was Hitachi Aloka α10 with a sampling frequency of 40 MHz. A linear probe, UST-5412, with 192 elements was attached to the diagnostic apparatus. The transmission frequency was 7.5 MHz. 96 elements were used in a single transmission and reception. The spacing between elements was 0.2 mm. The focal point for the transmission was set at 30 mm. No apodization was applied for transmission and reception.

Figure 3 shows a schematic diagram of the water-tank experimental system. First, the angular characteristics of scattering and reflection were measured. We measured a short axis of a tungsten wire as a scatterer and an acrylic block as a reflector. In the present paper, the muscle was assumed to be a scatterer and simulated by the wire. Bone was assumed to be a reflector and simulated by the surface of the acrylic block. The depth of these objects was set at $z_R = 30$ mm from the probe surface. The acrylic block was measured against the probe surface inclined from 0° to 15° with 1° step. This simulates the tilting of the thoracic spine against the skin surface. We obtained the scattering and reflection characteristics of the reference data, $R_S(\theta; z_R)$ and $\{R_R(\theta; z_R, \phi)\}$, as follows. First, the received element position and time where the enveloped amplitude was the largest among all the received elements was calculated. Second, the ideal delay time for each element was calculated referred to the position and time. Finally, the instantaneous value of the enveloped amplitude of each element was calculated at the ideal delay time. The number of sampling points was interpolated 8 times for the sampling of 40 MHz to calculate the angular amplitude characteristics with high accuracy.

Next, the thoracic spine of two healthy men in their 20 s was measured. The measurement section was set at paracentral visible the dura mater during the puncture. The measurements were applied while the patient was lied down and curled up as in the case of anesthesia. The depth and tilt of the thoracic spine for the subjects were 28–35 mm and 7°–11°, respectively.

3. Results and discussion

3.1. Result of water-tank experiment

Figure 4 shows the measured results of the scattering and reflection characteristics. The measurement result for the scatterer is shown in Figs. 4(a1)–4(c1) and that for the reflector when $\phi = 10°$ is shown in Figs. 4(a2)–4(c2). Figures 4(a1) and 4(a2) are the B-mode images, Figs. 4(b1) and 4(b2) are the amplitude data acquired at each element before the delay-and-sum processing on the yellow line in Figs. 4(a1) and 4(a2), and Figs. 4(c1) and 4(c2) are the amplitude values on the green dashed lines in Figs. 4(b1) and 4(b2). The green curvature is the ideal delay time of the scattered waves from a point scatterer. Comparing Figs. 4(c1) and 4(c2), low angle dependency in scattering characteristics and high angle dependency in reflection characteristics were confirmed. Figure 5 summarizes the measurement results of the angular amplitude characteristics. The red line is the scattering property and the blue and black lines are the reflection properties. As the slope of the reflector increases, the color of the line becomes bluer. We confirmed that the reflective properties shifted in the θ-axis direction according to the inclination of the reflector. The above results were consistent with those shown in Fig. 1.

We estimated which object was scatterer or reflector, and if it was a reflector how inclination it was using the angular amplitude characteristics in Fig. 5 as reference. The reflection properties from a negative slope reflector were calculated from those for positive slopes by reversing the properties for equal absolute values of the slope ϕ in the θ-axis direction. Figure 6 shows the results of the object estimation for the data acquired at the water-tank experiments. The result for the scatterer is shown in Figs. 6(a1)–6(c1) and that for the reflector when $\phi = 10°$ is shown in Figs. 6(a2)–6(c2). In these figures, Figs. 6(a1) and 6(a2) are the B-mode images,

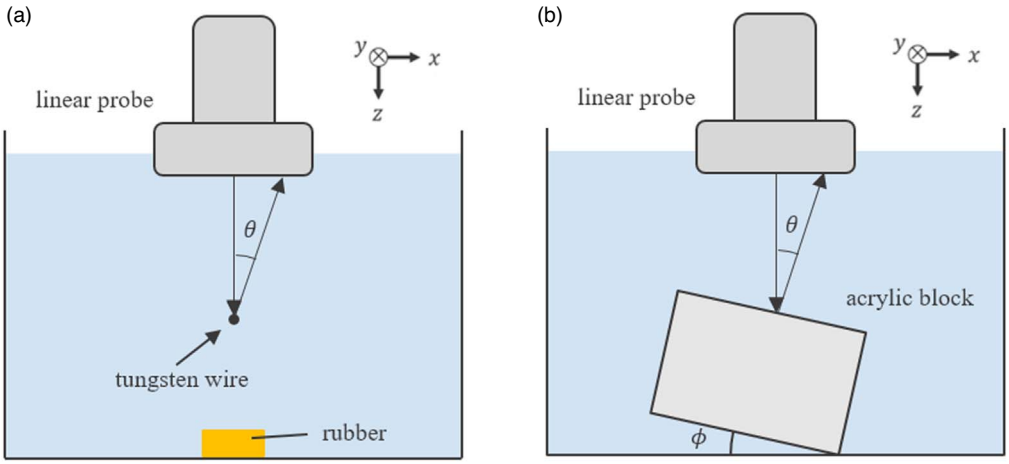

Fig. 3. (Color online) Schematic diagram of the water-tank experimental system. (a) Measurement of scattering characteristics. A very thin tungsten wire along the short axis direction was measured as a scatterer. (b) Measurement of reflective characteristics. The acrylic block was measured concerning the probe from 0° to 15°at the 1° step.

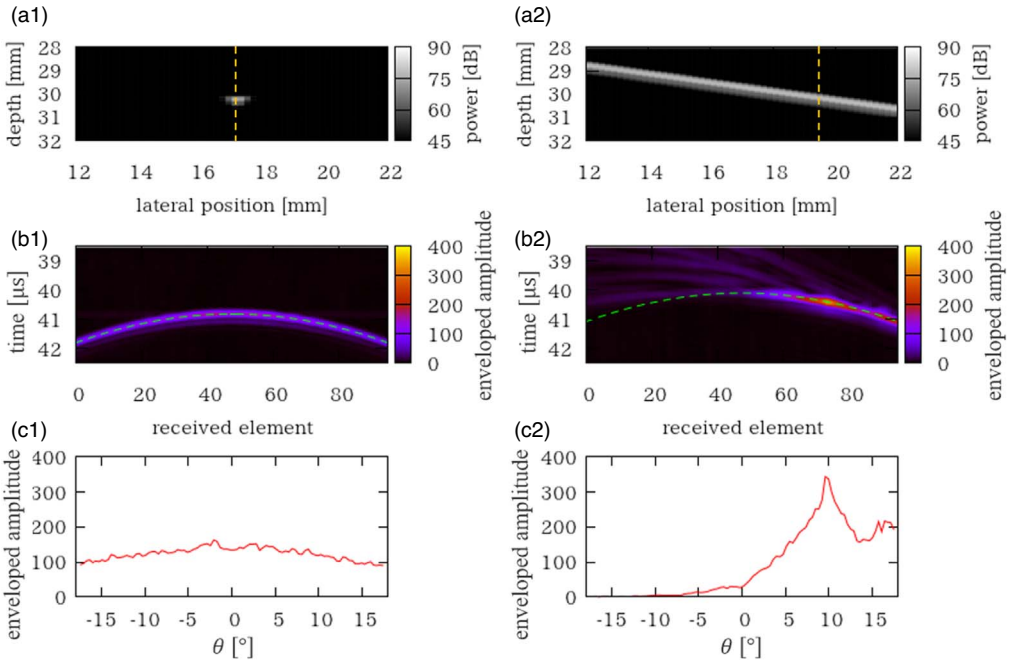

Fig. 4. (Color online) Results of the water-tank experiments. (a1)–(c1) Results for a scatterer, (a2)–(c2) results for a reflector, (a1), (a2) B-mode image, (b1), (b2) each element data, which is necessary for the image formation on the yellow dashed line of the B-mode image, and (c1), (c2) angular amplitude characteristics. We plotted the amplitude of the element data on the green line in (b1) and (b2), respectively.

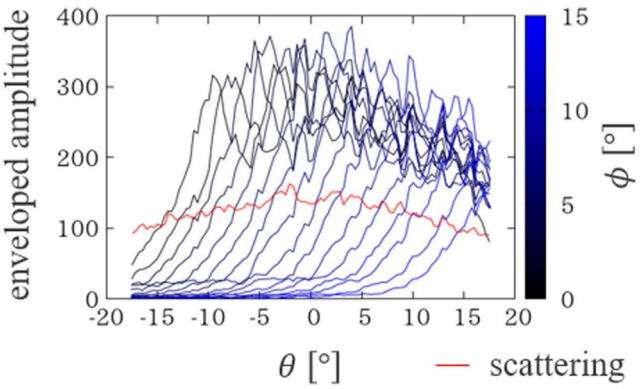

Fig. 5. (Color online) The angular amplitude characteristics measured in the water-tank experiments. The red line is the scattering property and the blue and black lines are the reflection properties.

6(b1) and 6(b2) are the matching results using the normalized cross correlation, and 6(c1) and 6(c2) are those using the RMSE. The estimated results were plotted with purple for the scatterer and the other colors for the reflector depending on the estimated slope. Comparing Figs. 6(b1) and 6(c1), almost all of the estimates were correct using the RMSE, but there were many misestimates using the normalized cross correlation. In Figs. 6(b2) and 6(c2), estimates by both methods were generally correct in estimating the reflectors.

3.2. Difference between normalized cross-correlation and RMSE

In this section, we compared the two matching methods. The estimated results for the scatterer using the normalized cross correlation differed from those using the RMSE. Here, we discuss the difference in the angular amplitude characteristics at the matching. For this discussion, we investigated the angular amplitude characteristics obtained at the black dot $P_0(x_0, z_R)$ shown in the scatterer estimation results in Figs. 6(b1) and 6(c1). The depth of P_0 was equal to the depth at which the scattering and reflection properties of the reference were acquired.

Figure 7(a) shows the amplitude angle characteristics obtained at the point $P_0(x_0, z_R)$ and some of the amplitude angle characteristics of the reference data. The point $P_0(x_0, z_R)$ should be estimated as a scatterer, as there was one scatterer at the depth equal to the focus of the transmitted beam. Figure 7(b) shows each angular amplitude characteristic normalized by the standard deviation after removing the DC component to calculate the normalized cross-correlation. Figure 7(d) shows the raw data of $R(\theta; P_0)$ and reference data $R_S(\theta; z_R)$ and $\{R_R(\theta; z_R, \phi)\}$ after multiplying each of them by the coefficient $\hat{A}_S(P_0)$ or $\hat{A}_R(P_0, \phi)$ to calculate the minimal RMSE between $R(\theta; P_0)$ and each reference data. Focusing on the characteristics of measured scattering (green line) and referred reflection in $\phi = 5°$ (blue line), they are very different in terms of angle dependence of amplitude in Fig. 7(a), although they are very similar in Fig. 7(b). In contrast, in Fig. 7(d), they are significantly different, as well as in Fig. 7(a). Figure 7(c) shows the calculated results of the normalized cross correlation between the amplitude angular characteristics at the point $P_0(x_0, z_R)$ and each reference data. The correlation with the reference data of the scattering property is shown with the dotted red line. Thus, the result by the normalized cross correlation did not provide the maximum correlation with the true value (scattering characteristics). Some positions in Fig. 6(b1) were also misestimated. When the normalized cross correlation is calculated, the DC component of the waveform is removed and the amplitude is normalized using the standard deviation. These two processes reduced the difference of angular dependence of the scattering and reflection characteristics, and false estimation was caused because the similarity between the scattering and reflection reference data became higher than that before the processing.

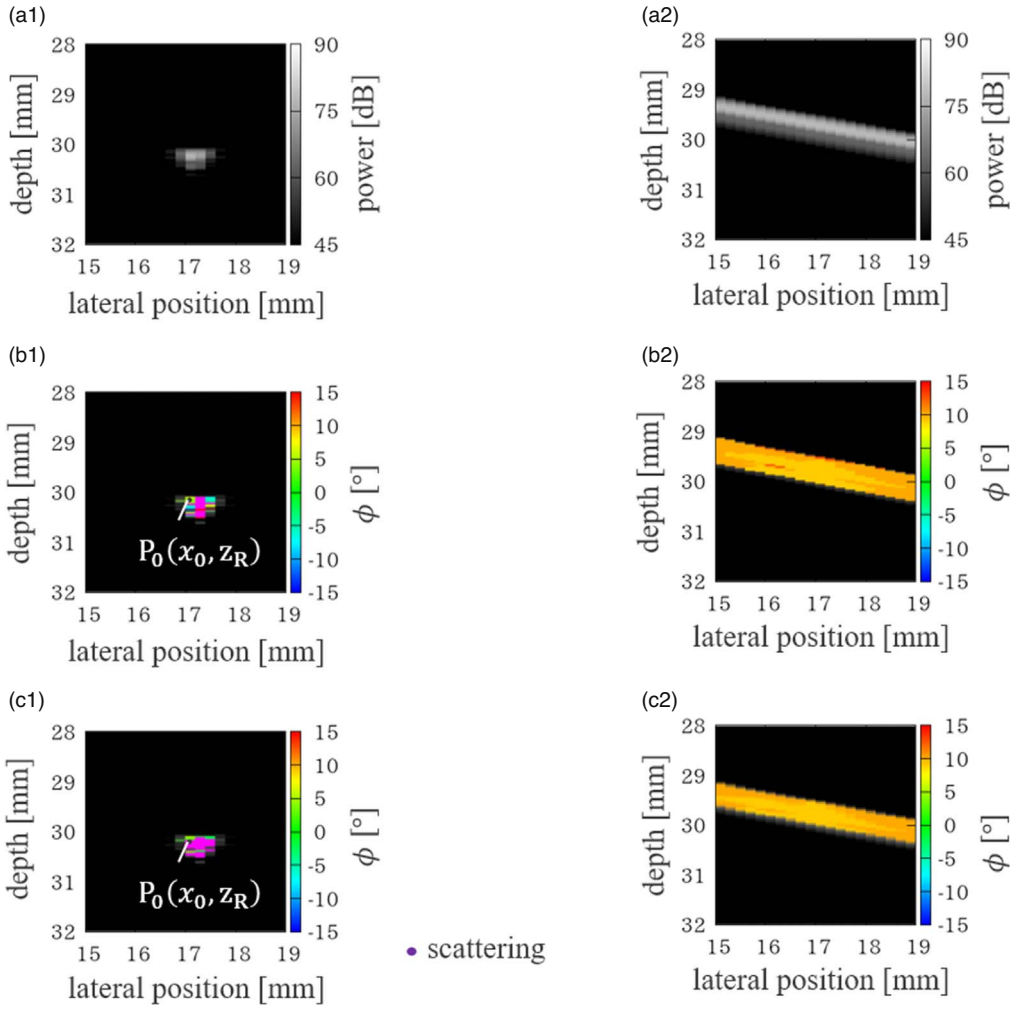

Fig. 6. (Color online) Results of object estimation using the data from the water-tank experiment. (a1)–(c1) Results for a scatterer, (a2)–(c2) results for a reflector, (a1), (a2) B-mode images, (b1), (b2) normalized cross-correlation matching, and (c1), (c2) RMSE matching.

On the other hand, when calculating the RMSE, we multiply the reference data by a constant value such that the RMSE is minimized. Figure 7(e) shows the calculated results of the RMSE with each reference data. Thus, the result using the RMSE was able to correctly estimate the scatterer in the position where misestimation occurred when using the normalized cross correlation since the RMSE retains information on the angular dependence of the amplitude angular characteristics as shown in Fig. 7(d).

3.3. Result of in vivo experiment

Figure 8 shows the measurement results of the human thoracic spine for two subjects A and B, respectively. In these figures, Figs. 8(a1) and 8(a2) are the B-mode images, 8(b1) and 8(b2) are the locations inferred to be bone and analysis area, 8(c1) and 8(c2) are the trivalued images with low-level brightness values, estimated positions as a scatterer, and estimated positions as a reflector, 8(d1) and 8(d2) are the RMSE results between the angular amplitude characteristics obtained at each point and the reference scattering characteristics by Eq. (6), and 8(e1) and 8(e2) are the matching results using RMSE. In Figs. 8(c1) and 8(c2), black points show the points where the brightness value was less than −30 dB of the maximum value in each B-mode image and the object estimation was not done at the points. Magenta points indicate the points where a scatterer is presumed to be located. Green points indicate where a reflector is presumed to be located. In Figs. 8(e1) and 8(e2), only the points estimated as the reflector were overlapped to the B-mode image.

The position and inclination of the bones were almost correctly estimated in both subjects for the estimation of bone. The result for subject A in Fig. 8(e1) was generally successful in differentiating the depiction of muscle tissue and bone because there were few points where muscle tissues above bone were estimated as the reflectors. However, the result for subject B in Fig. 8(e2) had many points where muscle tissues were estimated as the reflector. Moreover, in both subjects, muscle tissues were largely estimated as the reflector in the points on both sides of the images.

3.4. Discussion of in vivo result

Bones were almost estimated to be reflectors as well as the assumption. Although the muscle was assumed to be a scatterer, there were points where it was estimated to be a reflector, and there were differences in the estimated results between the two subjects. In particular, there were many points where the muscle was estimated to be a reflector in the edge of the transmitted beam. The number of elements available for transmission and reception was decreased for lateral positions of 0–8 mm and 28–36 mm. The reflection characteristics were changed by the lack of the number of

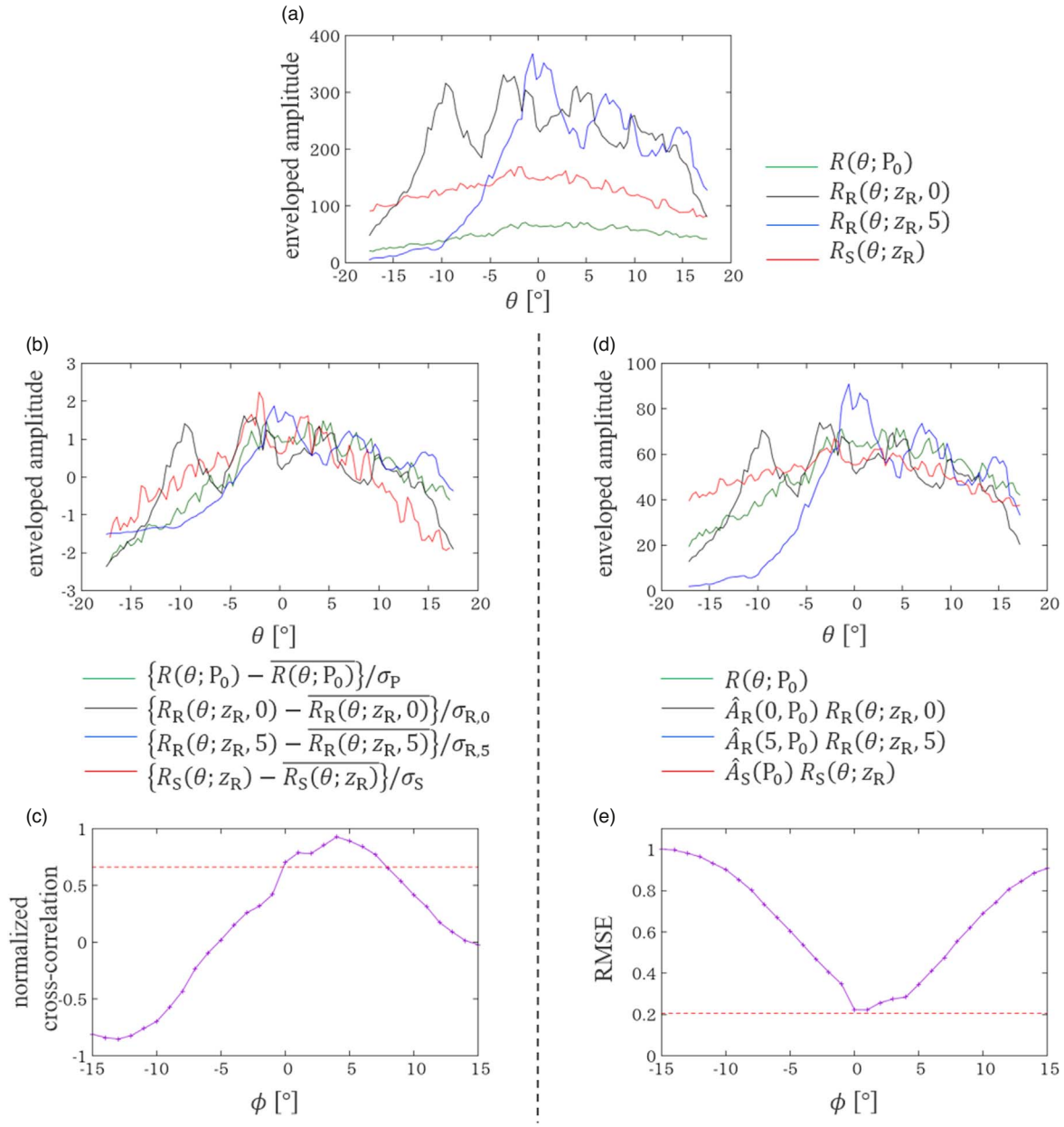

Fig. 7. (Color online) Amplitude angle characteristic at a position $P_0(x_0, z_R)$ where the results for the two matching methods differed. (a) The raw characteristics before processing, (b) the characteristics for computing the normalized cross correlation, (c) the values of the normalized cross correlation between $R(\theta; P_0)$ and each reference data. The red dotted line shows the correlation value between $R(\theta; P_0)$ and $R_S(\theta; z_R)$, (d) the characteristics for computing the RMSE, and (e) the RMSE value of $R(\theta; P_0)$ for each reference data. The red dotted line shows the RMSE value of $R(\theta; P_0)$ for $R_S(\theta; z_R)$.

elements for transmission. The estimation accuracy may be declined because the number of received data was decreased, especially for the large-θ data, where the difference between the scattering and the reflection is obvious, for matching. As shown in Figs. 8(d1) and 8(d2), the RMSE values of the angular amplitude characteristics from muscle tissues for the reference scattering characteristics were high on both sides.

To further investigate the results of muscle and bone estimation, the amplitude angular characteristics obtained for the muscle tissue and the bone for subject B are shown in Fig. 9. The green lines in Figs. 9(a) and 9(c) show the angular amplitude characteristics for the muscle tissue obtained at the point $P_1(x_1, z_1)$ in Fig. 8(b2) and the bone obtained at the point $P_2(x_2, z_2)$, respectively. The angular amplitude characteristic of the muscle tissue was expected to have the smallest error with the scattering characteristic shown by the red line in Fig. 9(a), however, the result for the refection characteristic with $\phi = -5°$ was the smallest in practice. Comparing to the scattering characteristic from a point scatterer, the angular amplitude characteristics from the muscle tissue showed greater attenuation of the amplitude at large $|\theta|$. We expected $RMSE_S(P)$ was large at the bone location and small at the muscle location, but as shown in Figs. 8(d1) and 8(d2), there was no difference in the value of $RMSE_S(P)$ between them to identify the bone location. There were two reasons for the difference in scattering characteristics between in vivo and water tank experiments. The first was the construction of muscle. Muscle tissue is composed of bundles of muscle fibers with 10–150 μm diameter and covered by fascia.[33] In the present paper, the muscle fibers were simulated by a single wire. Since the fascia is a plane structure and cannot be simulated by a wire, the angular amplitude characteristics

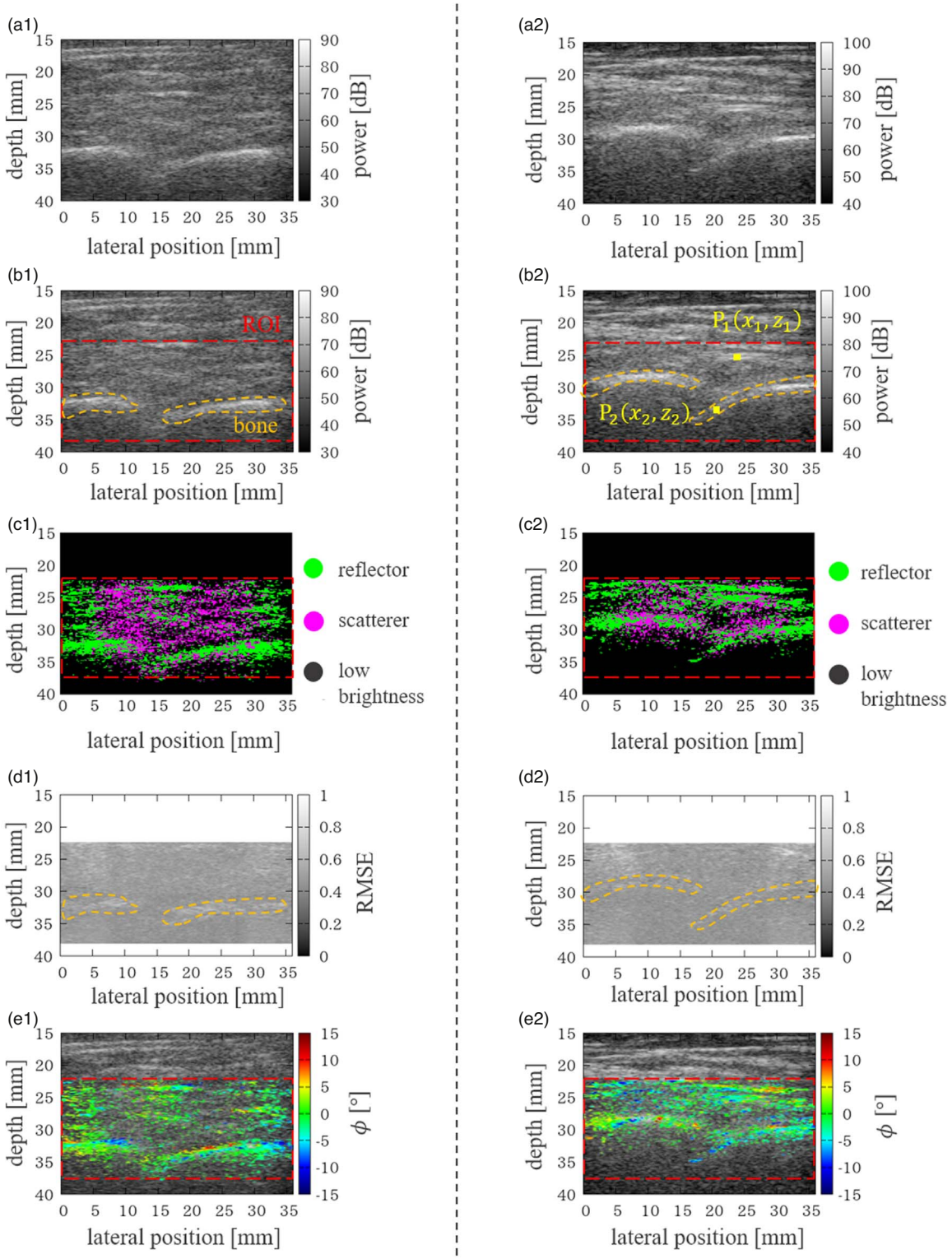

Fig. 8. (Color online) Results of applying the RMSE matching method to the human thoracic spine. (a1)–(e1) Subject A, (a2)–(e2) Subject B, (a1), (a2) B-mode image, (b1), (b2) analysis range and bone position, (c1), (c2) the image differentiating the depiction between scatterers and reflectors, (d1), (d2) RMSE values between angular amplitude characteristics obtained at each point and reference scattering characteristics, (e1), (e2) estimated result.

calculated from it may be different from the scattering characteristics of the water tank experiment. Also, the angular amplitude characteristics from the muscle fibers oriented in the direction of the long axis of the probe should be considered. The second was the wide width of the transmitted beam relative to the focal area at the shallower region. The depth of $P_1(x_1, z_1)$ is shallower than that of focus and thus the transmitted beam was not fully focused. As the beam width becomes wider, the effect of interference between reflected waves from objects at different locations within the beam width becomes larger.

On the other hand, the amplitude angular characteristics from the bone had a minimum RMSE with the reference data of $\phi = -8°$ from Fig. 9(d). The local slope of the bone at the point $P_2(x_2, z_2)$ was calculated from the RF signals, and its value was $-8.5°$, which agreed with the estimated results.

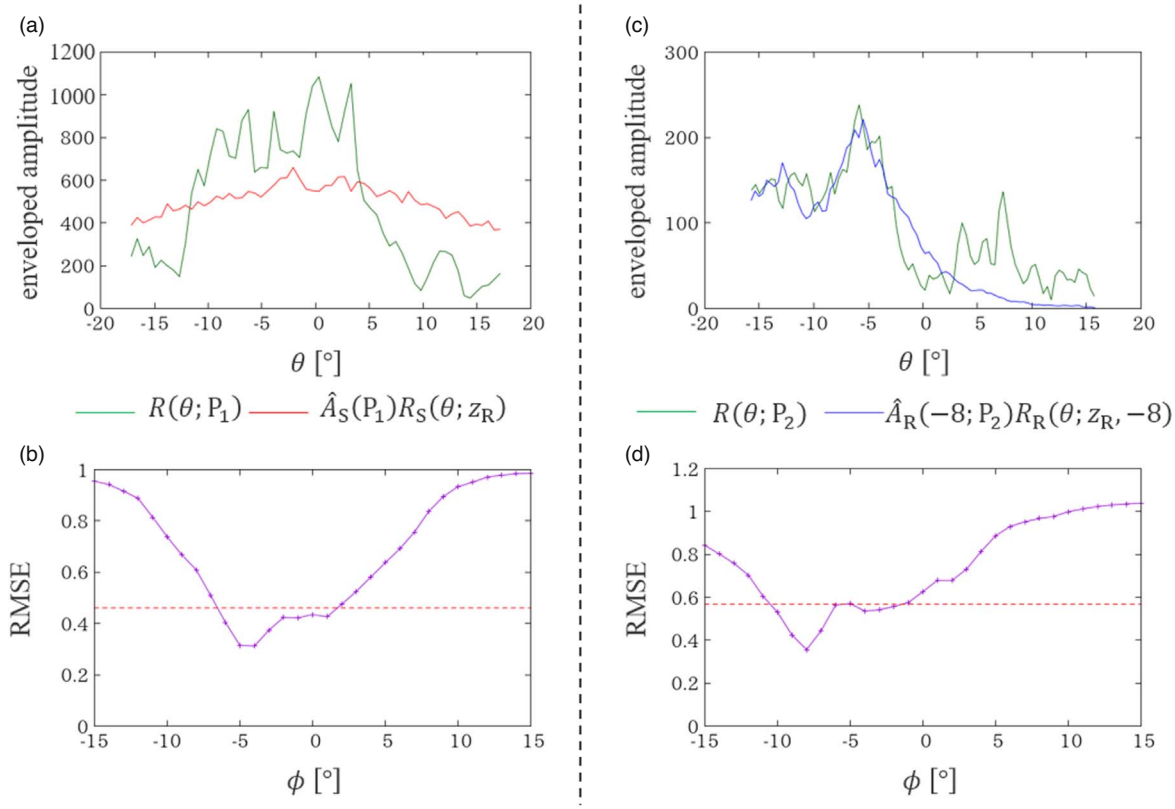

Fig. 9. (Color online) Amplitude angular characteristics and the matching results obtained for subject B. (a) The amplitude angular characteristics obtained for the point $P_1(x_1,\ z_1)$ in Fig. 8(b2) and the scattering reference data, (b) the RMSE values of $R(\theta;\ P_1)$ for each reference data, (c) the amplitude angular characteristics obtained from the point $P_2(x_2,\ z_2)$ in Fig. 8(b2) and the reference data for reflection with $\phi = -8°$, (d) the RMSE values of $R(\theta;\ P_2)$ for each reference data.

The angle estimation results of the bone were different in the depth direction in some parts, although those of the acrylic block were almost constant in the depth direction at all lateral positions. For example, the angle estimation result of the bone at the lateral position of 23.0 mm in Fig. 8(e1) showed that the estimation angles at the positions with low brightness were different from those at the high brightness positions. Figure 10 shows the relationship between the angle estimation results and the brightness values of the B-mode image at the lateral position of 23.0 mm in the depth of 32.6–33.6 mm in subject A. The red line (−5°) shows the estimated angle at this position from the B-mode image.

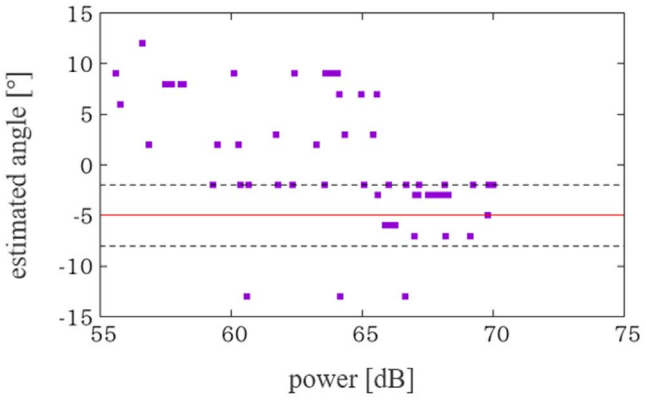

Fig. 10. (Color online) The relationship between the angle estimation results and the brightness values of the B-mode image at the lateral position of 23.0 mm in the depth of 32.6–33.6 mm of subject A.

The black dotted line shows the acceptable error range, where we assumed that is within ±3°. At the higher brightness positions, the angles were estimated as approximately −5°. However, the angles could not be correctly estimated at the lower brightness positions. A high signal-to-noise ratio would improve the accuracy of the angle estimation. In the future, we will further investigate the methods to acquire the accurate results of the angle estimation.

Differentiation between shallow muscle, especially fascia, and bone is required to detect the puncture position of the anesthetic needle. To solve this problem, the following studies are required in the future. (1) Measurements and analyses of the angular amplitude characteristics from muscle tissues located shallower than the focal point of the probe, (2) measurements and analyses of the amplitude angular characteristics for a single thin wire and a bundle of multiple wires, and (3) investigation of the best window function to calculate the RMSE. The suppression of muscle depiction has still a challenge, but the proposed method enabled us to emphasize bone depiction.

4. Conclusions

In the present paper, we proposed a depiction method using the difference in angular amplitude characteristics between scattering and reflection for the sharp depiction of the thoracic spine surface. The normalized cross correlation and the RMSE were used for the matching, and the results were compared. The use of the RMSE for the matching in the water-tank experiments allowed us to differentiate the

depiction of scattering and reflection. In the measurements for human thoracic vertebrae, the position and inclination of the bones were almost correctly estimated at the higher brightness position. To further suppress the depiction of muscle, weighting functions for calculating RMSE, the angular amplitude characteristics from the scatterers in a shallow region, and the difference in the angular amplitude characteristics between the single small scatterer and the aggregate of the multiple scatterers should be investigated. However, the ability to detect the reflection characteristics from the bone will greatly assist in thoracic epidural anesthesia in the future.

Acknowledgments

This work was partially supported by JSPS KAKENHI 20H02156.

1) R. D. Miller, N. H. Cohen, L. I. Eriksson, L. A. Fleisher, J. P. Wiener-Kronish, and W. L. Young, *Miller's Anesthesia* (Saunders, Amsterdam, 2015).
2) C. Konrad, G. Schupfer, M. Wietlisbach, and H. Gerber, Anesth. Analg. **86**, 635 (1998).
3) G. Le Coq, B. Ducot, and D. Benhamou, Can. J. Anaesth. **45**, 719 (1998).
4) M. P. N. Lewis, P. Thomas, L. F. Wilson, and R. C. Mulholland, Anesthesia **47**, 47 (1992).
5) B. T. Finucane and B. C. H. Tsui, *Complications of Regional Anesthesia* (Springer, New York, 2009).
6) M. Yamauchi, Trends Anaesth. Crit. Care. **2**, 234 (2012).
7) M. Nassar and I. A. Abdelazim, J. Clin. Monit. Comput. **29**, 573 (2015).
8) C. Alwin, Curr. Opin. Anaesthesiol. **33**, 674 (2020).
9) B. Grosse, S. Eberbach, H. O. Pinnschmidt, D. Vincent, M. Schmidt-Niemann, and K. Reinshagen, BMC Anesthesiol. **20**, 256 (2020).
10) J. A. Lim, S. Y. Sung, J. H. Lee, S. Y. Lee, S. G. Kwak, T. Ryu, and W. S. Roh, Medicine **99**, e21684 (2020).
11) T. Grau, R. W. Leipold, S. Delorme, E. Martin, and J. Motsch, Reg. Anesth. Pain Med. **27**, 200 (2002).
12) M. Tiouririne, A. J. Dixon, F. W. Mauldin Jr, D. Scalzo, and A. Krishnarai, Invest Radiol. **52**, 447 (2017).
13) H. Rafi-Tari, V. A. Lessowav, A. A. Kamani, P. Abolmaesumi, and R. Rohling, Ultrasound Med. Biol. **41**, 2220 (2015).
14) M. Pesteie, V. Lessowav, P. Abolmaesumi, and R. N. Rohling, IEEE Trans. Med. Imaging **37**, 81 (2018).
15) T. T. Oh, M. Ikhsan, K. K. Tan, S. Rehena, N. R. Han, A. T. H. Sia, and B. L. Sng, BMC Anesthesiol. **19**, 57 (2019).
16) N. Quader, A. Hodgson, and R. Abugharbieh, Conf. Proc. CLIP 2014, p. 76, 2014.
17) F. Ozdemir, E. Ozkan, and O. Goksel, Conf. Proc Medl Image Comput Asiist Interv., p. 256, 2016.
18) S. Yu, K. K. Tan, B. L. Sng, S. Li, and A. T. H. Sia, Proc. IEEE 12th Int. Symp. Biomed Imag, p. 243, 2015.
19) T. T.-Y. Lee, W. W. Jiang, C. L. K. Cheng, K. K.-L. Lai, M. K. T. To, R. M. Castelein, J. P. Y. Cheung, and Y.-P. Zheng, Ultrasound Med. Biol. **45**, 2725 (2019).
20) Y. S. Wong, K. K. L. Lai, Y. P. Zheng, L. L. N. Wong, B. K. W. Ng, A. L. H. Hung, B. H. K. Yip, W. C. W. Chu, A. W. H. Ng, and Y. Qiu, Ultrasound Med. Biol. **45**, 2866 (2019).
21) M. Matsukawa, Jpn. J. Appl. Phys. **58**, SG0802 (2019).
22) S. F. Eby, P. Song, S. Chen, Q. Chen, J. F. Greenleaf, and K.-N. An, J. Biomech. **46**, 2381 (2013).
23) M. A. Hussain, A. J. Hodgson, and R. Abugharbieh, Ultrasound Med. Biol. **43**, 648 (2017).
24) I. Hacihaliloglu, R. Abugharbieh, A. J. Hodgson, and R. N. Rohling, Ultrasound Med. Biol. **35**, 1475 (2009).
25) P. Pandey, N. Quader, K. Mulpuri, P. Guy, R. Garbi, and A. J. Hodgson, Epic Series in Health Sciences **3**, 301 (2019).
26) K. Takahashi, H. Taki, E. Onishi, M. Yamauchi, and H. Kanai, Jpn. J. Appl. Phys. **56**, 07JF01 (2017).
27) T. Sakamoto, H. Taki, and T. Sato, Acoust. Sci. Technol. **32**, 143 (2011).
28) S. Kidera, T. Sakamoto, and T. Sato, IEEE Trans. Geosci. Remote Sens. **48**, 1993 (2010).
29) H. Taki, S. Tanimura, T. Sakamoto, T. Shiina, and T. Sato, J. Med. Ultrason. **42**, 51 (2015).
30) T. Yokoyama, S. Mori, M. Arakawa, E. Onishi, M. Yamauchi, and H. Kanai, J. Med. Ultrason. **47**, 3 (2019).
31) T. Hashimoto, S. Mori, M. Arakawa, E. Onishi, M. Yamauchi, and H. Kanai, Proc. Symp. Ultrason. Electr. **41**, 2Pb5-3 (2020).
32) R. S. Bandaru, A. R. Sornes, J. Hermans, E. Samset, and J. D'hooge, IEEE Trans. Ultrason. Ferroelectr. Freq. Control **63**, 2057 (2016).
33) J. Feher, *Quantitative Human Physiology: An Introduction* (Academic, Amsterdam, 2012).